3D-Printed Submicron Patterns Reveal the Interrelation between Cell Adhesion, Cell Mechanics, and Osteogenesis

Nouri-Goushki, Mahdiyeh; Angeloni, Livia; Modaresifar, Khashayar; Minneboo, Michelle; Boukany, Pouyan E.; Mirzaali, Mohammad J.; Ghatkesar, Murali K.; Fratila-Apachitei, Lidy E.; Zadpoor, Amir A.

DOI
10.1021/acsami.1c03687

Publication date
2021

Document Version
Final published version

Published in
ACS Applied Materials and Interfaces

ACS APPLIED MATERIALS & INTERFACES

www.acsami.org

Research Article

3D-Printed Submicron Patterns Reveal the Interrelation between Cell Adhesion, Cell Mechanics, and Osteogenesis

Mahdiyeh Nouri-Goushki,* Livia Angeloni,* Khashayar Modaresifar, Michelle Minneboo, Pouyan E. Boukany, Mohammad J. Mirzaali, Murali K. Ghatkesar, Lidy E. Fratila-Apachitei,* and Amir A. Zadpoor

Cite This: *ACS Appl. Mater. Interfaces* 2021, 13, 33767−33781

Read Online

ACCESS | Metrics & More | Article Recommendations

ABSTRACT: The surface topography of implantable devices is of crucial importance for guiding the cascade of events that starts from the initial contact of the cells with the surface and continues until the complete integration of the device in its immediate environment. There is, however, limited quantitative information available regarding the relationships between the different stages of such cascade(s) and how the design of surface topography influences them. We, therefore, used direct laser writing to 3D-print submicron pillars with precisely controlled dimensions and spatial arrangements to perform a systematic study of such relationships. Using single-cell force spectroscopy, we measured the adhesion force and the work of adhesion of the preosteoblast cells residing on the different types of surfaces. Not only the adhesion parameters (after 2−60 s) but also the formation of focal adhesions was strongly dependent on the geometry and arrangement of the pillars: sufficiently tall and dense pillars enhanced both adhesion parameters and the formation of focal adhesions. Our morphological study of the cells (after 24 h) showed that those enhancements were associated with a specific way of cell settlement onto the surface (i.e., "top state"). The cells interacting with tall and dense pillars were also characterized by numerous thick actin stress fibers in the perinuclear region and possibly high internal stresses. Furthermore, living cells with highly organized cytoskeletal networks exhibited greater values of the elastic modulus. The early responses of the cells predicted their late response including matrix mineralization: tall and dense submicron pillars significantly upregulated the expression of osteopontin after 21 days of culture under both osteogenic and nonosteogenic conditions. Our findings paint a detailed picture of at least one possible cascade of events that starts from initial cell adhesion and continues to subsequent cellular functions and eventual matrix mineralization. These observations could inform the future developments of instructive surfaces for medical devices based on physical surface cues and early markers.

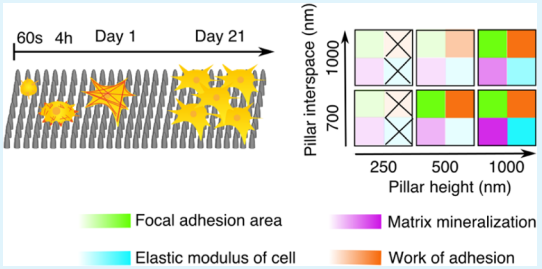

KEYWORDS: *biomaterials, surface patterns, cell adhesion, cell mechanics, osteogenic response*

1. INTRODUCTION

The micro- and nanotopographical features of a biomaterial surface influence cellular responses, including cell adhesion,[1] bactericidal activity,[2] and immunoregulatory effects.[3] The roles of a wide range of topographical characteristics in eliciting specific cellular responses have been investigated. These include surface roughness,[4] the aspect ratio of the surface features,[5] their shape, and dimensions,[6] which could be exploited to improve the treatment of bony defects. For example, micro- and nanostructured surfaces with certain characteristics have been found to promote the osteogenic response[7] of stem cells, thereby expediting the osseointegration and improving the service life of implants.

While the isolated effects of surface micro- and nanofeatures on the bone tissue regeneration process remain mainly elusive, some trends have already been identified. At the microscale (i.e., feature size > 1.0 μm), for example, surface micropillars with greater heights (i.e., ≥1.6 μm) and smaller diameters and interspacing (i.e., 1, 2, 4, and 6 μm) have been found to enhance the expression of osteogenic markers [e.g., osteopontin (OPN)].[8] At the nanoscale (i.e., feature size < 100 nm), previous studies[9,10] have reported a decreased level of OPN and osteocalcin (OCN) expression for nanopillars with greater heights. Despite the presence of these individual studies, the landscape of how the design parameters of surface patterns affect the osteogenic response remains largely unknown: (i) how the cell adhesion properties (e.g., cell adhesion work and force) are regulated via interactions with patterns at different

Received: February 25, 2021
Accepted: June 30, 2021
Published: July 12, 2021

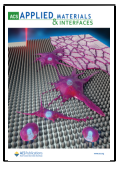

scales (from nano- to microscale) and (ii) whether the initial cell adhesion force promotes the osteogenic differentiation of the cells.

It is becoming increasingly clear that cellular receptors, such as integrins, can sense small topographical features during the adhesion phase and activate topography-induced mechanotransduction pathways.[11] These involve integrin clustering, the formation of focal adhesions (FAs), and the reorganization of the cytoskeleton and nucleus.[11,12] There are, therefore, many mechanobiological pathways that are directly or indirectly involved in how surface features influence cell response. Quantification of the adhesion force of the cell during its early interactions with patterned surfaces could enhance our understanding of how mechanics-related factors influence cell−surface interactions. However, most previous studies have used qualitative approaches, such as flow shear stress assays,[13,14] stretching devices,[11,15] and microscopy techniques,[16] to evaluate the adhesion of cells to the substrate.

Among experimental force-sensitive techniques for the mechanical probing of cells,[17] single-cell force spectroscopy (SCFS) can quantitatively measure the early stage[18] of cellular adhesion force in the range of a few to tens of nanonewtons[19] while precisely manipulating the cell attachment positions. To date, few studies have applied SCFS to measure the initial cellular adhesion force of osteoblasts[18,20−22] and mesenchymal stem cells (MSCs)[19,23] on various surfaces. Quantitative SCFS analyses have revealed that the adhesion force of the human osteoblasts increases with the surface roughness on selected laser-melted titanium surfaces, reaching a value of 8.5 nN on the roughest surface relative to surfaces treated with different blasting agents.[20] This finding was associated with a higher degree of osteoblast colonization. In another SCFS study, partially denatured collagen surfaces were found to increase the initial cellular adhesion relative to native collagen and promote spreading, migration, and osteogenic differentiation of preosteoblasts.[18]

SCFS has not yet been applied to surfaces decorated with precisely controlled micro- and nanopatterns. Understanding the impact of the design parameters of surface micro- and nanopatterns and their length scale on cell adhesion and the interrelation between the adhesion forces and subsequent cell functions necessitates systematic studies of such effects.[24] One of the main factors that limit such systematic investigations has been the unavailability of fabrication methods for creating precisely controlled patterns. Direct laser writing via two-photon polymerization (2PP) has been recently shown to be a powerful technique for generating submicron patterns with high degrees of reproducibility and geometric fidelity.[25,26] Moreover, this technique facilitates the surface engineering of implantable devices since it is capable of printing structures with a wide range of length scales (i.e., 200 nm−100 mm) in a single-step process. In our previous studies,[25,26] we have demonstrated the 3D printing of highly controllable submicron patterns over a large area and the cytocompatibility of the applied materials (IP-DIP and IP-L780) for the human MSCs (hMCSs) and MC3T3-E1 preosteoblast cells.

To reveal the relationships between the various steps of cell−surface interactions and to identify the early markers of the osteogenic potential of surface-decorated biomaterials, we studied the effects of height and interspace of submicron pillars on the response of MC3T3-E1 cells from the adhesion phase up to matrix mineralization under both osteogenic and nonosteogenic conditions. Toward that aim, we applied quantitative methods, such as SCFS, atomic force microscopy (AFM), as well as a host of biological assays. Particular attention was paid to the spatiotemporal changes in cell morphology, cytoskeletal organization, the formation of FAs, and the mechanical characterization of living cells during the adhesion phase (from few seconds to 24 h). Moreover, the relevant properties of the patterns (dimensions, wettability, and roughness) and the cell−pattern interface were assessed to better elucidate the underlying mechanisms.

2. MATERIALS AND METHODS

2.1. Fabrication of the Patterns. Submicron pillars with a diameter of 250 nm, different heights (i.e., 250, 500, and 1000 nm), and interspaces (i.e., center-to-center distances of 700 and 1000 nm) were designed and printed using a Photonic Professional GT machine (Nanoscribe, Germany) following our previously described protocol.[25] Briefly, six different patterns were designed and imported into a job preparation program (Describe, Nanoscribe, Germany). Arrays (1.0 mm^2) of pillars were manufactured with a laser power of 14% and a scanning speed of 1200 μm/s using the conventional configuration and the galvo writing strategy. A droplet of IP-L780 resin (Nanoscribe, Germany) was placed on a glass coverslip and then exposed to a femtosecond infrared laser beam (wavelength of 780 nm) to fabricate the designed patterns. After printing, the specimens were developed in propylene glycol monomethyl ether acetate (Sigma-Aldrich, Germany) and rinsed in isopropyl alcohol (Sigma-Aldrich, Germany) for 25 and 5 min, respectively, followed by blow-drying.

We refer to the patterns with a "small" interspace (designed value = 700 nm) with the letter "S" and the patterns with a "large" interspace (designed value = 1000 nm) with the letter "L". The lowest height (designed value = 250 nm) will be identified with the number "1", the intermediate height (designed value = 500 nm) with the number "2", and the highest height (designed value = 1000 nm) with the number "3". Thus, groups S1, S2, and S3 were patterned using a "small" (i.e., 700 nm) interspace and the designed heights of 250, 500, and 1000 nm, respectively. Similarly, groups L1, L2, and L3 were patterned with a "large" (i.e., 1000 nm) interspace and the designed heights of 250, 500, and 1000 nm, respectively. For all groups, the flat substrate (glass) was considered as the control group.

2.2. Characterization of the Patterns. *2.2.1. Morphological Analysis.* The morphology of the patterns was characterized by using scanning electron microscopy (SEM) (Helios Nano Lab 650, FEI, USA). The specimens were coated with gold (coating thickness ≈ 5 nm) using a sputter coater (JFC-1300, JEOL, Japan) and then imaged by SEM. To acquire the height of the pillars, the samples were tilted 30° during imaging. The average diameter and height of 100 pillars from the different areas of each sample were quantified using ImageJ (http://rsb.info.nih.gov/ij/index.html). The reported height values of the pillars were corrected for the measurement tilt angle.

3D topographical images of the patterns were acquired in the tapping mode using an atomic force microscope (JPK Nanowizard 4, Germany) and a high aspect ratio probe (TESPA-HAR, Bruker, Germany). Three images of 10 μm × 10 μm for each sample were recorded and analyzed. The average surface roughness (R_a) was determined using the JPK SPM data processing software (JPK instruments, v6.1, Germany).

2.2.2. Wettability. The wettability of the patterned surfaces was measured using a drop shape analyzer (KRUSS DSA100, Germany). Briefly, deionized water droplets (2.0 μL) were placed on the flat (glass without patterns) and patterned surfaces (with an area of 9.0 mm^2), and the contact angle was recorded after 5 s (n = 3) at room temperature.

2.2.3. Surface Chemistry Analysis. Fourier transform infrared spectroscopy (FTIR, Thermo Fisher Scientific Nicolet FTIR spectrometer 6700, US) was performed to identify the functional group of the IP-L780 photoresist and the submicron pillars. Four scans in the range of 4000−650 cm^{-1} were performed to acquire each spectrum using the attenuated total reflection (ATR) element.

https://doi.org/10.1021/acsami.1c03687
ACS Appl. Mater. Interfaces 2021, 13, 33767−33781

X-ray photoelectron spectroscopy (XPS, Thermo Fisher K-Alpha, Rockford, IL, USA) was performed to analyze the chemical composition of the 3D-printed submicron pillars on the glass substrate. Ten scans were acquired with an energy step of 0.2 eV using an Al Kα source gun with a spot size of 400 μm^2 in the standard lens mode. Due to the small size of the pillars and the space between the individual pillars, XPS measured both the pillars and the substrate. The apparent disturbance of the potassium (K 2p) signal within a carbon (C 1s) scan was used to calculate and subtract the amount of the carbon signal that originated from the substrate.

2.3. Cell Experiments. *2.3.1. Cell Culture Conditions.* The specimens were first sterilized by immersion in 70% ethanol (Sigma-Aldrich, Germany), followed by UV light exposure for 20 min. Then, 5.0×10^4 preosteoblast cells (MC3T3-E1, Sigma-Aldrich, Germany, passage 11) were seeded on each sample in a 6-well plate (Greiner Bio-One, Netherlands) and incubated at 37 °C, 5% CO_2 (Life Technologies, US) in an alpha minimum essential medium (α-MEM) (Thermo Fisher, US) supplemented with 10% (v/v) fetal bovine serum (Thermo Fisher, US) and 1% (v/v) penicillin−streptomycin (Thermo Fisher, US). For the long-term experiments (i.e., 21 days of culture), the medium was refreshed every 2 days. For the cases where osteogenic conditions were desired, ascorbic acid and β-glycerophosphate (both from Sigma-Aldrich, Germany) were added to α-MEM (1:1000 and 1:500, respectively) from day 2.

2.3.2. Cell Adhesion Measurements by SCFS. SCFS experiments were performed using a JPK Nanowizard IV AFM (JPK Instruments, Germany) mounted on a Zeiss Axio Observer optical microscope (Carl Zeiss AG, Germany) and equipped with the JPK CellHesion module (JPK Instruments, Germany), which allows for an extended 100 μm Z-range. The specimens were glued to Petri dishes (TPP, Switzerland), which were compatible with the JPK Petri dish heater (JPK Instruments, Germany) that maintained the temperature constant at 37 °C during the experiments.

Arrow TL-tipless cantilevers (NanoWorld, Switzerland) with a nominal spring constant of 0.03 N/m were incubated in phosphate-buffered saline (PBS, Thermo Fisher, US) containing 10 μg/mL fibronectin (Sigma-Aldrich, Germany) for 30 min at room temperature. After functionalization, the cantilevers were rinsed twice in PBS and were calibrated using the thermal noise method.

For the SCFS experiments, 5.0×10^4 MC3T3-E1 cells were precultured in a standard 6-well plate. When the cells reached confluence, the culture medium was removed, and the cells were rinsed twice with 2.0 mL of PBS and were detached from the well using 100 μL of 0.5% trypsin−ethylenediaminetetraacetic acid (Thermo Fisher Scientific, US) solution (37 °C, 3 min). The trypsinized cells were suspended in 1.0 mL of culture media and were used for the SCFS experiments. 100 μL of the cell suspension was directly injected in a Petri dish containing the sample and 2.0 mL of culture medium, relatively far from the patterned area. Single round cells were identified by the optical microscope and were individually picked up by the functionalized probe. To pick the cells, the free end of the cantilever was carefully aligned with the cell, and a force−distance cycle was performed using the following parameters: (i) a setpoint force of 3 nN, a Z length of 50 μm, an approach and retract speed of 2 μm/s, and a contact time of 10 s. The cantilever with a cell attached to the tip is referred to as the "cell probe". The cell adhesion measurements with surfaces were then performed by acquiring force−distance curves with the "cell probe" using the following parameters: (i) a setpoint force of 1 nN, a Z length of 80 μm, and an approach/retract speed of 5 μm/s. Since the first phase of cell adhesion, characterized by single-integrin adhesion events, takes place during the first 60 s of contact with a surface,[27−29] 2 and 60 s contact times were tested.

Since immunostaining analysis showed that cells interacting with L1 and S1 patterns did not have different behaviors (in terms of cell area, cell morphology, and FAs) as compared to the control samples, SCFS experiments were performed only on S2, S3, L2, and L3 and on the control (flat glass) surfaces. Three force−distance curves on the pattern and three force−distance curves on the glass control surface were acquired with each "cell probe". Between seven and nine cells were tested on each specimen. The reported normalized values of the adhesion force and the work of adhesion were obtained by normalizing the values from each cell on the patterns to the values obtained for the same cell on the glass control surface. The nonparametric Kruskal−Wallis test was used to compare the measurements obtained on the different patterns.

2.3.3. Immunocytochemistry Analyses. The actin filaments, nucleus, and FAs of the cells were stained after 4 h and 1 day. As previously described,[25] the specimens were first rinsed with PBS, and the cells were fixed using a 4% (v/v) formaldehyde solution (Sigma-Aldrich, Germany). After permeabilization with 0.5% Triton X-100/PBS (Sigma-Aldrich, Germany) at 4 °C for 5 min, the cells were incubated in 1% BSA/PBS (Sigma-Aldrich, Germany) at 37 °C for 5 min. Then, the specimens were incubated in the rhodamine-conjugated phalloidin (1:1000 in 1% BSA/PBS, Thermo Fisher, US) and antivinculin mouse monoclonal primary antibody (1:100 in 1% BSA/PBS, Sigma-Aldrich, Germany) for 1 h at 37 °C. The cells were then rinsed thrice with 0.5% Tween-20/PBS (Sigma-Aldrich, Germany) and incubated in Alexa Fluor 488, donkey antimouse polyclonal secondary antibody (1:200 in BSA/PBS, Thermo Fisher, US) for 1 h at room temperature. The specimens were again rinsed thrice with 0.5% Tween-20/PBS for 5 min each time, followed by 5 min rinsing with 1× PBS. Afterward, a droplet of 10 μL of ProLong gold (containing 4′,6-diamidino-2-phenylindole, Thermo Fisher, US) was laid on the cells, and the specimens were flipped over on microscopic glass slides and were imaged using a fluorescence microscope (ZOE fluorescent cell imager, Bio-Rad, the Netherlands).

For SEM observations, the stained specimens were rinsed twice with distilled water for 5 min and were dehydrated in 50, 70, and 96% ethanol solutions for 15, 20, and 20 min, respectively. Finally, the samples were dried overnight at room temperature and were coated with gold by sputtering prior to being imaged by SEM.

The cell matrix mineralization was analyzed on day 21 in both nonosteogenic and osteogenic media. Therefore, the cells were washed with PBS and were fixed with a 4% (v/v) formaldehyde solution for 15 min. Next, the samples were prepared for staining by a process similar to cytoskeleton staining (see above). The cells were incubated with the OPN antibody conjugated to Alexa Fluor 488 (1:100 in BSA/PBS, Santa Cruz Biotechnology, US) for 1 h at 37 °C. Then, the cells were rinsed thrice with 0.5% Tween-20/PBS for 5 min, followed by a subsequent 5 min rinsing with 1× PBS. ProLong gold was added to the specimens, and they were mounted on glass slides to be imaged using the fluorescence microscope.

2.3.4. Mechanics of Living Cells by AFM. Mechanical mapping of living cells after 1 day of culture was performed using an atomic force microscope (JPK Nanowizard III, JPK Instruments, Germany) in the quantitative imaging mode and a qp-BioAC-CB3 probe (Nanosensors, Switzerland) with a nominal spring constant of 0.06 N/m. The instrument allowed for a maximum scan area of 30 μm × 30 μm. During the experiments, the temperature was maintained at 37 °C using the JPK Petri dish heater (JPK Instruments, Germany). The probe was calibrated using the thermal noise method.[30] The applied setpoint force was 1 nN, which corresponded to an indentation depth in the range of 300−900 nm. The cells were evaluated using a pixel time of 20 ms and a Z length of 2.0 μm. The maps of the elastic modulus were obtained by fitting the force−distance curves measured at each point of the scanned area to the Hertz−Sneddon model[31] considering a paraboloid tip with a nominal tip radius of 10 nm. The reported values of the elastic modulus were calculated as the average elastic modulus value in a certain area of interest (e.g., the periphery or center of the cells).

2.3.5. Image Analysis. ImageJ was used to process the fluorescence images. First, the image overlay was split into channels to separate the nucleus, F-actin, and other proteins (i.e., vinculin and OPN). The grayscale images of F-actin and OPN were thresholded. The cell area, the degree of anisotropy (DA, $DA \sim 1$ presents polarization in cells and $DA \sim 0$ indicates the fully isotropic cells) of 20 cells per sample ($n = 4$), and the OPN area ($n = 4$) were then quantified through the Analyze Particle command.[25]

https://doi.org/10.1021/acsami.1c03687
ACS Appl. Mater. Interfaces 2021, 13, 33767−33781

Table 1. Characteristics of the Submicron Pillars, the Printing Times, and the Average Roughness of the Patterned Surfaces

	diameter [nm]		interspacing [nm]		height [nm]		aspect ratio	density [/100 μm^2]	print time [h/mm^2]	roughness (R_a) [nm]
groups	design	measured	design	measured	design	measured	design	design	measured	measured
S1	250	235 ± 16	700	716 ± 12	250	251 ± 24	1	205	5.5	79 ± 13
S2	250	288 ± 9	700	714 ± 9	500	540 ± 46	2	205	7.5	114 ± 2
S3	250	305 ± 14	700	706 ± 9	1000	928 ± 32	4	205	11.5	236 ± 11
L1	250	211 ± 21	1000	1012 ± 13	250	253 ± 30	1	100	4.5	29 ± 2
L2	250	265 ± 17	1000	1010 ± 14	500	498 ± 28	2	100	5.5	91 ± 8
L3	250	297 ± 4	1000	1012 ± 15	1000	973 ± 44	4	100	7.5	213 ± 13

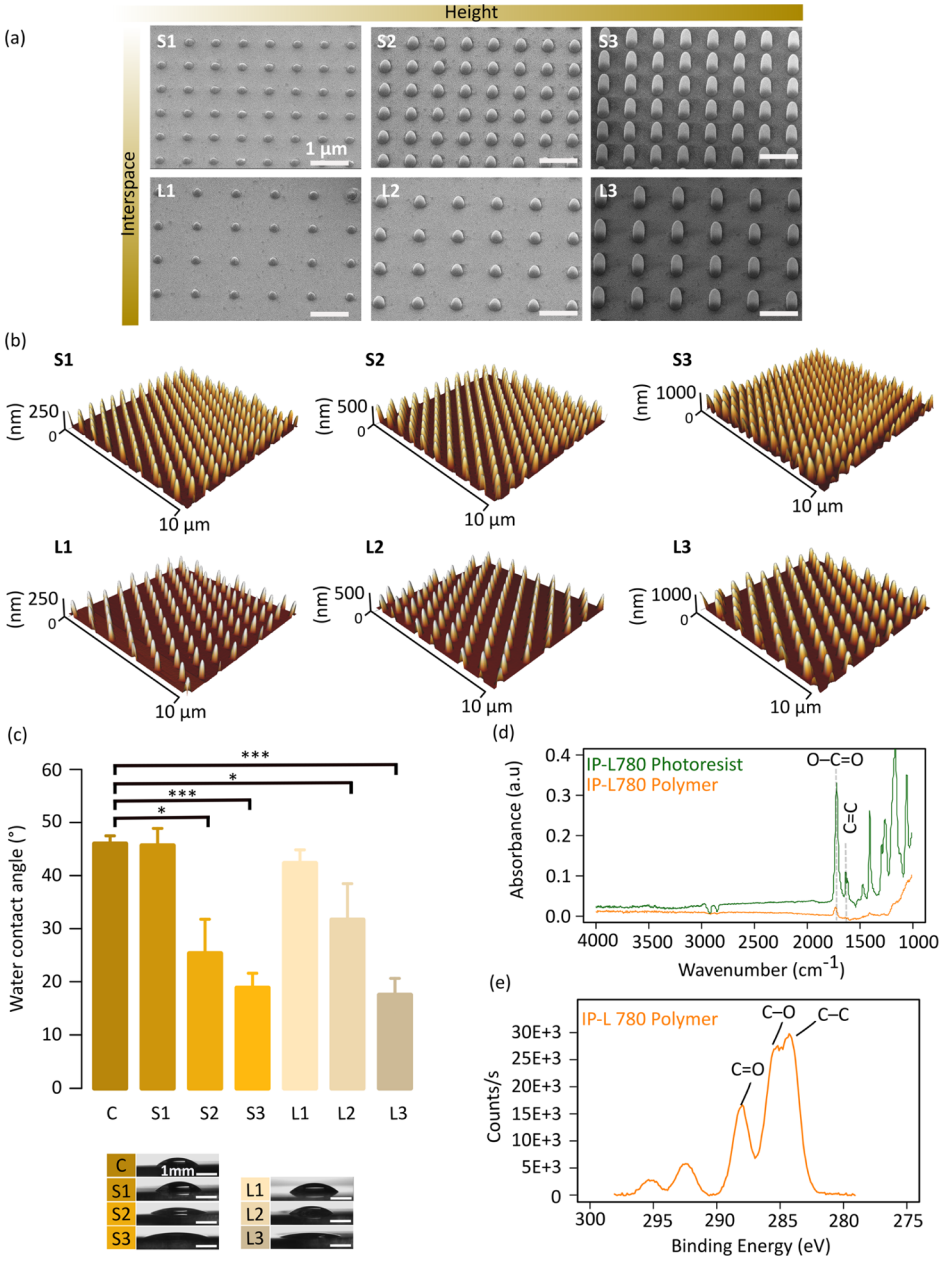

Figure 1. Characterization of the submicron pillars. (a) SEM and (b) AFM images of submicron pillars 3D-printed using 2PP. (c) Comparison of the wettability of the patterned and control (glass) (C) specimens characterized through water contact angle measurement (*p < 0.05, **p < 0.01, and ***p < 0.001). (d) FTIR spectra in the ATR mode of the IP-L780 photoresist and polymer (after 2PP). (e) XPS spectra of C 1s peaks in IP-L780 after polymerization.

To count and measure the FA area, a previously described method was used.[32] Briefly, the background was subtracted from the grayscale images under the sliding paraboloid option with a rolling ball radius of 50 pixels. The local contrast of the image was then enhanced by running the CLAHE plugin (https://imagej.nih.gov/ij/plugins/clahe/index.html) with a block size of 19, histogram bins of 256, and a maximum slope of 6. To further minimize the background, the mathematical exponential (EXP) was applied through the process

https://doi.org/10.1021/acsami.1c03687
ACS Appl. Mater. Interfaces 2021, 13, 33767−33781

menu. Next, the brightness, contrast, and threshold were automatically adjusted. Finally, the area and number of FAs were measured using the Analyze Particle command.[32] The measurements were performed only on fully separated focal points. The unpaired *t*-test with Welch's correction was used to determine the significant level of difference with cells on the control sample (flat glass).

2.3.6. Statistical Analysis. To determine whether there were significant differences between the means of different experimental groups, one-way ANOVA followed by Tukey's multiple pairwise-comparisons *post-hoc* test was performed using Prism (version 8.0.1, GraphPad, CA, USA). A *p*-value below 0.05 was considered to indicate a statistical significance.

2.4. Computational Models. We used a commercial nonlinear finite element code (Abaqus, v6.21) for our computational simulations to study the mechanics of the submicron pillars interacting with cells. We used isotropic linear elastic material properties for the modeling of the submicron pillars (E = 3.35 GPa, ν = 0.4) and the glass substrates (E = 63 GPa, ν = 0.2). Using a tie-constraint, the pillar and the substrate were attached. Two pillars with different heights (h = 500 and 1000 nm) and similar boundary conditions were modeled. A reference point was defined at the center of the top surface of the pillars. This reference point was kinematically coupled to the nodes on the top surface of the pillars. A displacement boundary condition along the x-axis (U_x) was applied to the reference point. The magnitude of the displacement of the tip of the bent pillars was extracted from SEM images of the cells on different patterns using ImageJ. The displacements of the pillars were applied to the pillars present in each computational model (i.e., U_x = 0−70 nm for h = 500 nm and U_x = 0−190 nm for h = 1000 nm). Clamped boundary conditions were applied to the glass substrate. 3D quadratic hexahedral elements (C3D20) with a minimum mesh size of 20 nm were used in all of our models. A standard nonlinear analysis was used for the simulations. The average local traction forces were calculated from the experimental displacement observations.

3. RESULTS AND DISCUSSION

3.1. Characterization of the Patterns. The diameter and the interspacing of the pillars were generally very controllable (Table 1, Figure 1a). The deviations observed in the height of the pillars could be attributed to the fluctuations of the laser intensity during the printing process, as previously reported.[25,26] The printing time varied between 4.5 and 11.5 h/mm^2 depending on the height and areal density of the pillars (Table 1). The average roughness (R_a) of the series S and L was measured by AFM and varied between 79−236 and 29−213 nm, respectively (Table 1). As expected, the surface roughness increased with the height of the pillars, while increasing the interspacing of the pillars reduced the measured roughness of the patterned surface, particularly for the pillars with the smaller heights (Table 1, Figure 1b). The hydrophilicity of the substrate increased with the height of the pillars (Figure 1c). This behavior is in agreement with the previous studies[33,34] that have shown that rougher surfaces tend to increase the wettability of the surface if the contact angle of the initial surface (48° in our study) is below 60°.

We have analyzed the functional groups of photoresists before and after polymerization via the FTIR test. C═C stretch bonds were found in the region of 1680 cm^{-1} in the resin but disappeared in the polymer spectrum, indicating no signs of monomer after polymerization (Figure 1d). Peaks at 1720 cm^{-1} showed the ester groups in IP-L780 before and after polymerization (Figure 1d). Since polymerized nanopillars are printed over a small area, the absorbance value of the ester peak in the polymer is less than the one appearing in the monomer. Furthermore, we have quantified the binding energy and percentage of carbon bonds in the polymerized IP-L780 (Table 2). C−C, C═O, and C−O bonds were present in the XPS spectra of nanopillars showing the presence of acrylic structures in the polymer (Figure 1e).

Table 2. Energy Binding of C 1s Species in the 3D-Printed Submicron Pillars (Made of IP-L780)

bond	energy binding [eV]	atomic %
C−C	284.9	33.1
C−O	286.2	43.4
C═O	288.8	23.5

3.2. Differential Effects of the Patterns on Cell Adhesion, Morphology, and Elastic Modulus. *3.2.1. Cell Adhesion.* The representative force−distance (F−D) curves acquired at 2 and 60 s on the S2, S3, L2, and L3 patterns (Figure 2a) showed the typical shape observed when a cell interacts with a surface, indicating the proper functioning of our "cell probes" in terms of cell viability and the positioning of the cantilever. The maximum force peak on the retrace curve, indicating the cell detachment force (i.e., F_{adh}), was followed by step-like events, which were preceded either by a ramp-like change in force (jumps) or by a plateau region (tethers).[27,35,36]

The adhesion force (F_{adh}) and the work of adhesion (W_{adh}) increased for all groups after 60 s of contact time as compared to the values recorded after 2 s of contact. This can be explained by the fact that a longer contact time enables the formation of more and possibly stronger (more mature) adhesion sites between the cellular receptors and the surface. The type of pattern also influenced the cellular adhesion (Figure 2b,c). After both 2 and 60 s of contact time, the patterns with the tallest pillars (i.e., S3 and L3) exhibited significantly higher F_{adh} as compared to the patterns with the shorter pillars (i.e., S2 and L2) and the control surface (Figure 2b). The F_{adh} values measured for the S2 and L2 groups were not significantly different from those of the control surface (Figure 2b).

Furthermore, the patterns with the highest areal density of pillars (i.e., S3 and S2) exhibited a higher W_{adh} as compared to the patterns having similar heights but lower areal densities (i.e., L3 and L2). S3 exhibited higher W_{adh} as compared to L3 (Figure 2c). A less clear difference was observed between S2 and L2 where S2 exhibited slightly (but not significantly) higher W_{adh} as compared to L2 after both 2 and 60 s of contact time.

The curves acquired for the patterns with similar heights (and comparable roughness and contact angle) indicated similar values of F_{adh} after 60 s (e.g., 3.8 nN for S2, 4.8 nN for L2, 8.1 nN for S3, and 9.8 nN for L3 in the examples reported in Figure 2a). The adhesion force increased almost linearly with the height of the pillars. For example, the adhesion force corresponding to a pillar height of 1000 nm was around 2 times higher than the one corresponding to a pillar height of 500 nm. The work of adhesion, W_{adh}, was higher on the surfaces decorated with the denser patterns (e.g., 47.5 fJ for S2 vs 20.6 fJ for L2 and 43.5 fJ for S3 vs 33.8 fJ for L3 in the examples reported in Figure 2a).

In summary, the pattern with the tallest and densest pillars (S3) exhibited the highest values of the adhesion parameters (i.e., adhesion force and adhesion work). The L3 pattern, which has a similar height of pillars but a lower pillar density, exhibited an adhesion force that was similar to S3 but a lower work of adhesion. By comparison, the adhesion characteristics

https://doi.org/10.1021/acsami.1c03687
ACS Appl. Mater. Interfaces 2021, 13, 33767−33781

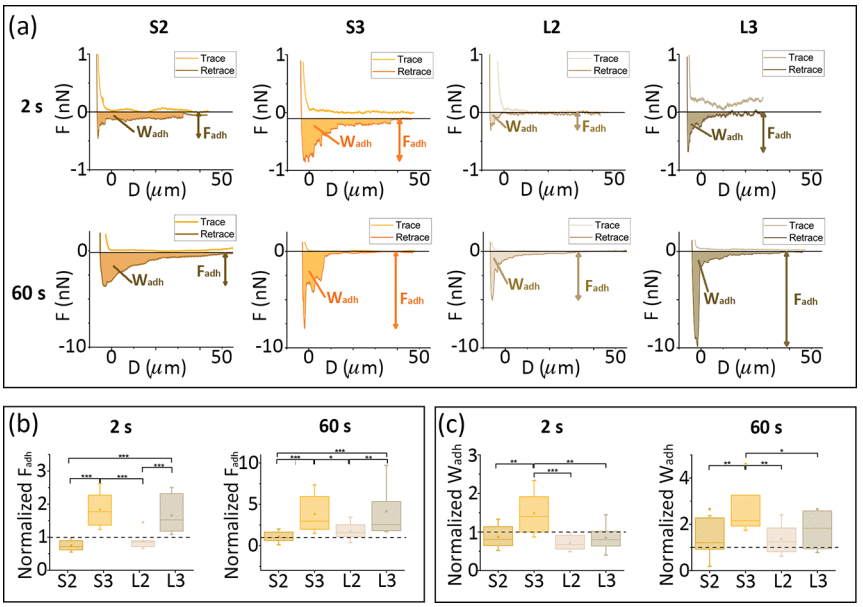

Figure 2. Characterization of cell adhesion: (a) representative F−D curves obtained by SCFS on S2, S3, L2, and L3 patterns after 2 s (first line) and 60 s (second line) of contact. (b) The adhesion force (normalized with respect to that of the control surface) was measured by SCFS on the patterned surfaces after 2 s (left) and 60 s (right) of contact. (c) Work of adhesion (normalized with respect to that of the control surface) measured by SCFS on the patterned surfaces after 2 s (left) and 60 s (right) of contact. The nonparametric one-way ANOVA (Kruskal−Wallis) test was used to evaluate the statistical significance of the differences between the various experimental groups (*$p < 0.1$, **$p < 0.05$, and ***$p < 0.01$).

of the shorter S2 and L2 patterns were close to the control surface with S2 showing a slightly higher work of adhesion as compared to L2 and the control group.

Hydrophilicity and roughness are known to impact the initial attachment of cells to various kinds of nonpatterned surfaces.[18,20,37,38] We found that the patterns with the tallest pillars (S3 and L3), which are also the most hydrophilic and roughest patterns (Figure 1c), result in the highest values of the adhesion force.

The interspacing between the pillars affected the mechanism of the early adhesion of cells to the analyzed submicron patterns: lower interspacing resulted in a greater work of adhesion. The work of adhesion depends, among such factors as the adhesion force and the characteristics of the cell type, on the number of the anchoring points (i.e., detachment events) of the cell to the surface.[36] Our results, therefore, suggest that the number of cellular anchoring points on the patterns increases with the areal density of the pillars. This increase was particularly clear for the patterns with the tallest pillars (i.e., S3 as compared to L3).

3.2.2. Cell Morphology and Cytoskeleton Organization. After 4 h of culture, round cells with an average area of 1900 ± 719 μm^2 and diameters around 49 μm were visible on all the patterns and the control specimens (Figure 3a,c). Nevertheless, the cells on the S3 pattern developed clearly visible membrane extensions rich in vinculin, indicating their ability to more easily spread and interact with the pillars on this pattern. Therefore, the largest variation in the cell area was encountered for this pattern (Figure 3c). The presence of relatively well-developed membrane extensions (mainly lamellipodia) around the periphery of the cells (Figure 3a) suggests the start of FA maturation, followed by the formation of actin bundles, indicating that the cells are in the contractile spreading phase.[39] On the contrary, the cells cultured on the control specimens and the specimens from other groups had nascent vinculin sites around the periphery of the cells and the protrusive activity was not yet started (Figure 3a), indicating that the cells were not yet in the contractile spreading phase[39] but rather in an earlier phase of the development of FAs.[39]

The faster development of FAs on the substrates exhibiting high hydrophilicity and initial adhesion force (measured by SCFS experiments) has been observed in studies performed on nonpatterned surfaces as well.[18] In our case, the formation of FAs on the S3 pattern was promoted not only by enhanced hydrophilicity but also by a higher areal density of pillars relative to the other patterns (e.g., L3) that could favor integrin clustering.[37] This was also supported by our SCFS experiments (Figure 2), which indicated that a high areal density of the pillars results in the formation of more discrete attachment sites already after 2 s and 1 min of contact with these patterned surfaces. Furthermore, integrin clustering may have been further favored by the lower stiffness of the taller pillars in the case of the S3 pattern. Indeed, taller pillars could undergo enhanced bending, thereby further approaching each other when subjected to the interaction forces with the cells.[40]

After the first day of culture, the cells significantly grew in size regardless of the experimental group (Figure 3b,c). The cells cultured on the patterned surfaces were, however, smaller than those residing on the control surface. In both S and L series, the cell area decreased with the height of the pillar from ≈ 2800−2900 μm^2 for the shorter pillars (S2 and L2) to ≈ 2100−2200 μm^2 for the taller pillars (L3 and S3). By comparison, the pillar interspacing did not affect the area of the cells (Figure 3b,c). This observation is in line with the previous studies that have reported a decrease in the cell area for an increased roughness in the submicron range.[4]

On day 1, the area and density of FAs per cell increased with the height of the pillars (Figure 3d,e). However, the pillar interspacing did not significantly influence the area and density of vinculin-rich plaques. The cells cultured on the S2, S3, and L3 specimens formed the largest FA areas with an average area of 6.5 ± 0.03 μm^2, which was significantly higher than the one

https://doi.org/10.1021/acsami.1c03687
ACS Appl. Mater. Interfaces 2021, 13, 33767−33781

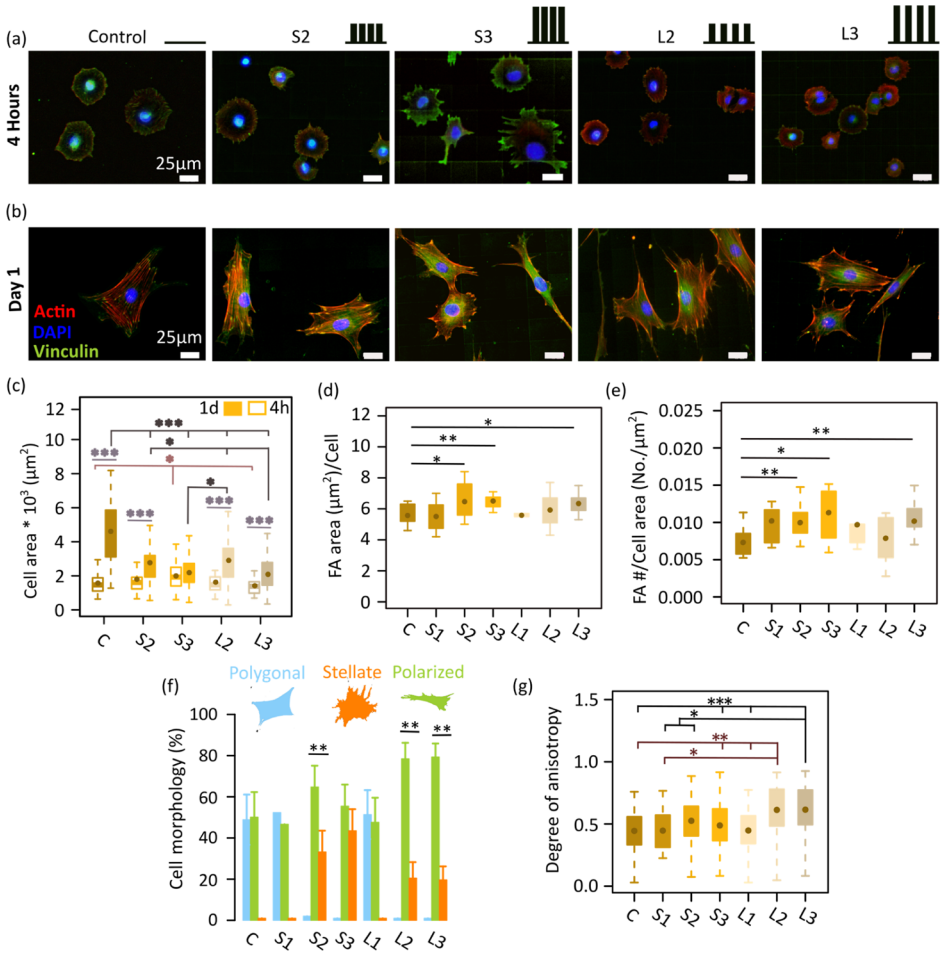

Figure 3. Cells spreading and the early response of the MC3T3-E1 cells cultured on the patterned and control surfaces at different time points. (a,b) F-actin, vinculin, and nucleus of the cells cultured on the control and different patterned surfaces after 4 h (b) and 1 day. (c) The cell areas were measured on the patterned and control samples after 4 h and 1 day. (d,e) FA area and FA density of the cells residing on the patterned and control surfaces on day 1. (f,g) Different types of cell morphology and the *DA* of the cells residing on the patterned and control surfaces on day 1 (*$p < 0.05$, **$p < 0.01$, and ***$p < 0.001$).

found on the control sample (i.e., 5.5 ± 0.7 μm^2) (Figure 3d). Furthermore, the cells residing on taller patterns (S3 and L3) exhibited the highest FA density (Figure 3e).

After 1 day of culture, three different cell shapes with different cytoskeletal organizations were visible on the specimens (Figure 3b,f): (1) polygonal cells with peripherally organized actin fibers, (2) polarized cells with perinuclear actin cap fibers, and (3) stellate cells characterized by the presence of actin fibers in the perinuclear region and multidirectional membrane extensions (mostly filopodia). The polygonal cells were isotropic (*DA* ∼ 0.4) and were found on the control specimens as well as on the specimens from the S1 and L1 groups (Figure 3b,f,g). The majority of the cells residing on the S2, L2, and L3 specimens were polarized (*DA* ∼ 0.7) with wider leading edges, showing the motile behavior of the cells (Figure 3b,f,g). The cells grown on the S3 pattern adopted a half-polarized, half-stellate morphology and had a *DA* value close to 0.5 (Figure 3b,f,g). In the stellate cells, F-actin stress fibers were stretched toward the protrusions and FA sites. Taken together, the *DA* and the number of polarized cells were enhanced as the height and interspacing of the pillars increased. However, the influence of the pillar interspacing on the shape and the *DA* of the cells was more pronounced than that of the height (Figure 3f,g).

Cells with different morphologies exhibited qualitatively different spatial organizations of the FAs and F-actin bundles (Figure 3b). A coupling between the FAs and the F-actin bundles was more visible for the cells with multidirectional protrusions (e.g., stellate cells on S3 and L3 in Figure 3b), which exhibited mature and long-lasting FA sites mainly at the proximity of the cell edge (mostly present in the S3 group) (Figure 3b). The coupling of F-actin with FAs around the periphery of cells tends to enhance cellular adhesion.[41] The coupling of vinculin with the actin bundles was less visible on the polarized cells than on the stellate cells, and they were mainly located in the front and rear of the cells (Figure 3b). On the polarized cells, the actin stress fibers were aligned and stretched along the direction of the protrusions, suggesting that the cells were migrating and indicating a higher destabilization of the cell adhesion as well as presumably short-lasting FA points.[42]

Furthermore, we observed three different settling states of the cells on the patterned surfaces (Figure 4a,b) that we categorized as follows: (i) a "top state"[43] in which the entire cell body resides on top of the submicron pillars, (ii) a "bottom state"[43] in which the submicron pillars fully penetrate the cell body, and (iii) a "mixed state"[43] where some areas of the cell

https://doi.org/10.1021/acsami.1c03687
ACS Appl. Mater. Interfaces 2021, 13, 33767−33781

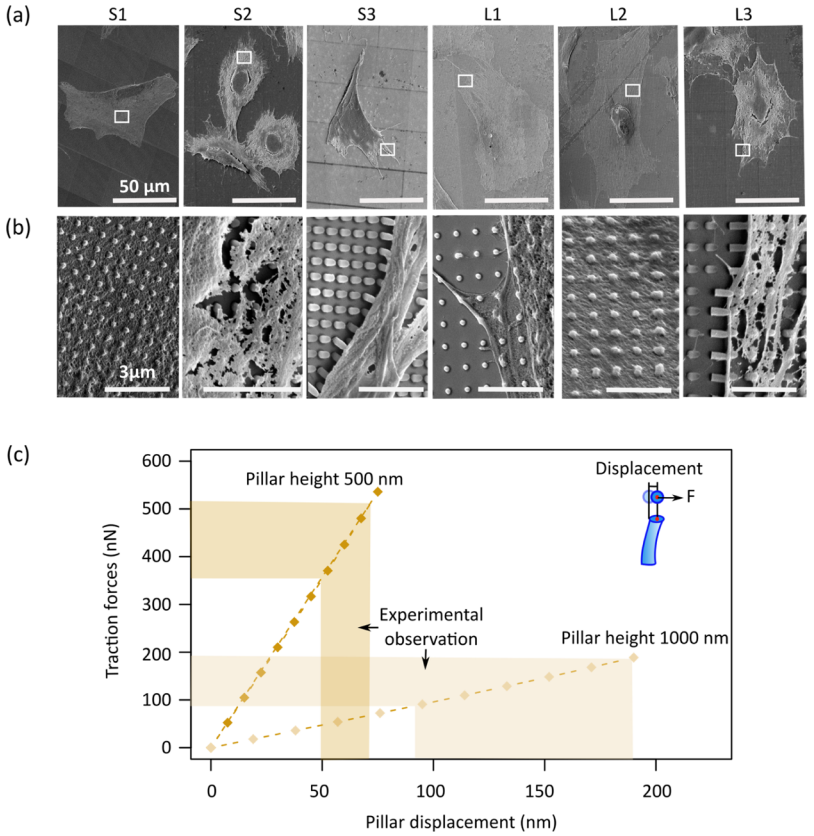

Figure 4. Visualization of the cell interactions with the patterned surfaces using SEM and computational modeling. (a,b) Low- and high-magnification SEM images of the cells on the patterned surfaces. (c,d) Reaction force (applied by cells to the pillars) and von Mises stress in the submicron pillars calculated using the computational models. Lateral displacements of 58, 140, and 289 nm were applied to the pillars with the heights of 250, 500, and 1000 nm, respectively.

sink into the submicron pillars (bottom state), whereas other areas reside on top of the pillars (top state) (Figure 4a,b).

On the shortest pillars (i.e., S1 and L1), the bottom state was observed. The cells fully engulfed the pillars and came into contact with the entire available surface of the pillars (top and lateral) and the substrate (Figure 4a,b). The body of the cells appeared very thin as the tip of the pillars was almost visible through the entire cell (Figure 4a,b). The pillar interspacing did not influence the settling state on those two patterns.

On the taller pillars, the effects of the pillar interspacing on the cell settling state were more pronounced. The cells cultured on the S2 patterns exhibited a mixed state, with a dominant top state. Indeed, the bottom state was observed only in some regions at the periphery of the cell. Moving toward the nucleus, the cell body appeared thicker, resulting in a top state (Figure 4a,b). On the L2 patterns, the bottom state was dominant and was observed almost for the entire body of the cells (Figure 4a,b). This may have been caused by the larger pillar interspacing, which helps the cells to easily fill the space between the submicron pillars.

In the case of the S3 patterns characterized by the maximum height and the minimum interspacing, the top state was always observed, suggesting that the cells come into contact only with the top of the pillars without touching the substrate (Figure 4a,b). On the L3 patterns, with the maximum height and interspacing, the mixed state was observed. The bottom state was observed only in very small regions around the cell periphery, especially at the rear and front ends of the cells, while the top state was dominant for the rest of the cell body (Figure 4a,b).

Previous studies have already shown the effects of the density of nanostructures on how cells "settle" onto a patterned surface and have demonstrated that a high areal density of nanostructures (ρ (/100 μm^2) $\geq$ 80) and a large diameter of nanopillars ($d \geq 200$ nm) energetically promote the top state.[43−45] The small interspacing between the nanopillars leads to intense stretching and unfolding deformation of the cell membranes while they adhere to the sidewalls.[43] Consequently, the cells adhere to the tip of the pillars. Here, we observed a combined effect of both the density and height of the pillars with a diameter of 250 nm. Indeed, both the height and interspacing in the range investigated in this study had an impact on the interactions between the cells and the underlying pillars. The cells that were cultured on the pillars with smaller heights and large interspacing distances (i.e., S1, L1, and L2) came into contact with both pillars and substrate (the dominant bottom state), while increasing the height of the pillars and decreasing their interspacing (i.e., S2, L3, and S3 patterns) caused the cells to mostly interact with the top of the pillars without touching the substrate, hence the dominant top state.

Interestingly, the cells were able to bend the pillars locally after 1 day of residing on the substrate. The bending was more prominent in the vicinity of the edge of the cells settled in the top state (S2, S3, and L3 in Figure 4a,b). The pillars were deflected toward the center of the cells (S2, S3, and L3 in Figure 4a,b). The lateral displacement of the pillar tips was

https://doi.org/10.1021/acsami.1c03687
ACS Appl. Mater. Interfaces 2021, 13, 33767−33781

measured by analyzing the SEM images of the dehydrated cells on the patterns (Figure 4c). The corresponding local traction forces in the proximity of the cell border were estimated through computational modeling (Figure 4c). The cells applied average local traction forces of 144 ± 38 nN to the pillars with a height of 1000 nm. A higher force value (429 ± 62 nN) was calculated for the pillars with a height of 500 nm. As the traction forces are exerted to the extracellular matrix by FAs,[46] we further assessed the relationship between the traction forces and the FA area. Although we observed no significant differences between the area of FAs on the pillars and the heights of 1000 and 500 nm, the estimated local traction forces were different on those pillars (height 500 and 1000 nm). These findings suggest that mature FAs with the same area can withstand a wide range of force values (100−429 nN estimated in Figure 4c), and the results of refs 46 and 47 support our findings. These observations were made for preosteoblasts and are in line with the previous studies that have found direct correlations between the FA size and the traction forces only during the initial growth phase of FAs and not for mature FAs.[46,47] It is, nevertheless, important to realize that the fixation protocol might affect the deformation of the pillars and thus the estimated forces.

3.2.3. Elastic Modulus of the Cells. The different shapes and cytoskeletal organizations found on the different patterns together with the observations on the cell−pattern interfaces indicated that cells residing on different patterns may also have different mechanical properties. Therefore, the elastic moduli of the living cells interacting with the patterned (S2, S3, L2, and L3) and control surfaces were analyzed by acquiring AFM mechanical maps of the cells after 1 day of culture (Figure 5). Exploiting the capability of AFM-based stiffness measurements to perform subsurface imaging of soft biological samples up to a depth of 900 nm[48,49] also allows for a more detailed analysis of the organization of cortical actin, especially in the perinuclear region.

On the control surfaces (Figure 5a,b), the presence of thick peripheral actin fibers was observed in the cells with both polygonal and polarized shapes, while no or few perinuclear actin fibers were detected. This type of cytoskeletal organization resulted in a high elastic modulus at the periphery of the cells (E = 25.8 kPa for the polygonal cell in Figure 5a and E = 42.5 kPa for the polarized cell shown in Figure 5b) and a low elastic modulus at the center of the cells, corresponding to the perinuclear region (E = 6.1 kPa in the case of the polygonal cell in Figure 5a and E = 4.9 kPa for the polarized cell in Figure 5b).

On all the patterned surfaces, the cells with the polarized shape presented aligned (almost parallel) fibers crossing the perinuclear region of the cells from the leading edge to the cell rear, suggesting a motile state where, in general, actin fibers tend to align in the direction of cell movement. This type of cytoskeletal organization can be ascribed to the actin cap formation[50] and gave rise to an elastic modulus, in the perinuclear region, in the range of 6−8 kPa for the cells cultured on the S2, L2, and L3 patterns (i.e., E = 7.6, 6.1, and 6.2 kPa for the cells shown in Figure 5d,h,j, respectively). A significantly higher elastic modulus in the perinuclear region was observed for the elongated cells residing on the S3 pattern (e.g., E = 14.45 kPa for the region shown in Figure 5f), which may be due to a more organized cytoskeleton formed by the thick bundles of actin fibers. This organization can be the result of a faster formation of perinuclear stress fibers in the

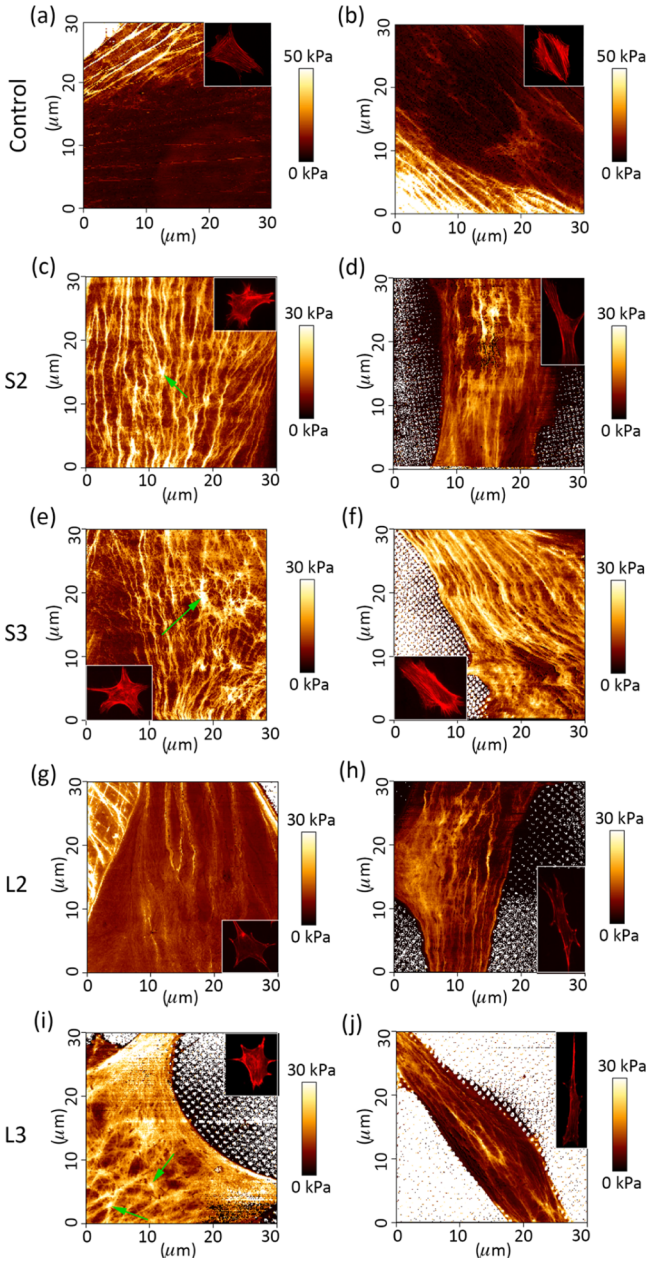

Figure 5. AFM-based mechanical characterization of the cells cultured on the patterned and control surfaces on day 1. Some examples of the maps of the elastic modulus obtained for a polygonal cell on the control surface (a), a polarized cell on the control surface (b), stellate cells on the S2, S3, L2, and L3 patterns (c,e,g,i), and polarized cells on the S2, S3, L2, and L3 patterns (d,f,h,j), respectively.

polarized cells grown on the S3 pattern and suggests higher cell contractility and tension.

Stellate cells exhibited a different type of cytoskeletal organization in the perinuclear region, which in the case of the specimens from the S2, S3, and L3 groups resulted in a branched network of thick bundles of actin fibers and thus higher values of the elastic modulus (E = 14.6, 13.9, and 14.5 kPa, respectively, for the cells residing on the S2, S3, and L3 patterns, Figure 5c,e,i). This type of organization indicates that the stress fibers in these cells were stretched in different directions. The presence of actin star sites (e.g., the small green arrows in Figure 5c,e,i) were associated with the highest values of the elastic modulus and suggested the entanglement of

https://doi.org/10.1021/acsami.1c03687
ACS Appl. Mater. Interfaces 2021, 13, 33767−33781

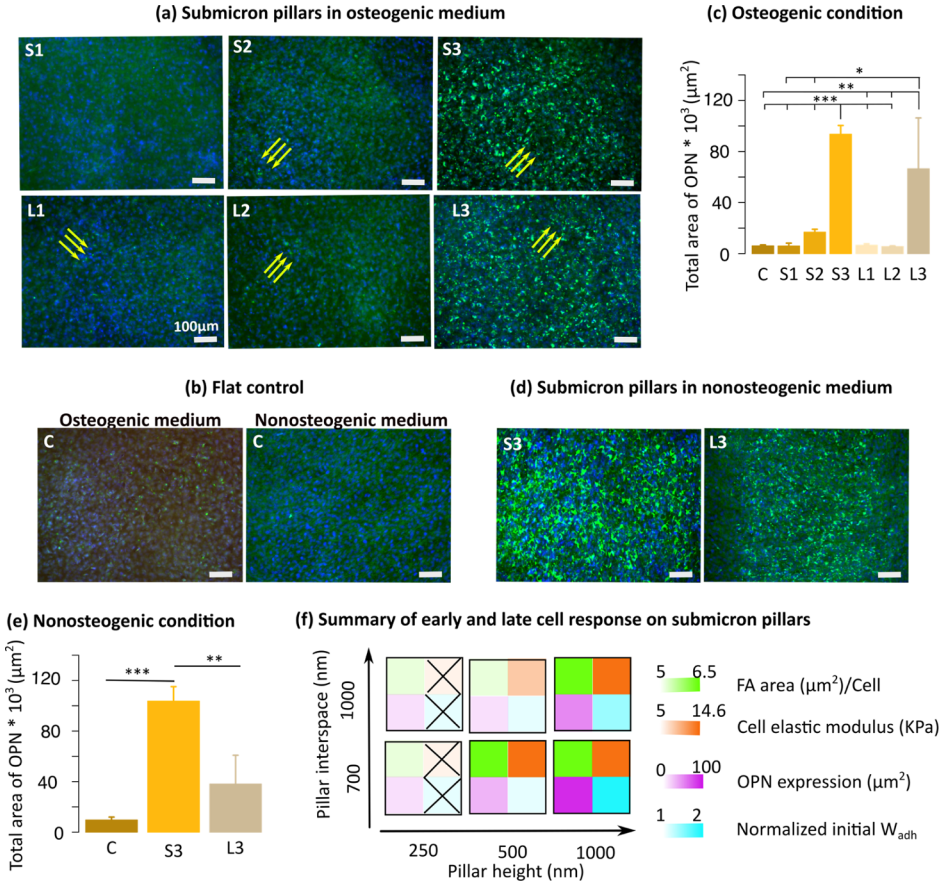

Figure 6. OPN expression in the MC3T3-E1 matrix after 21 days of culture. The experiments were performed under both osteogenic (a,c) and nonosteogenic (d,e) conditions. (b) Expression of OPN on the flat control in both osteogenic and nonosteogenic media. (f) Response of the preosteoblast cells as a function of the height and interspacing of the pillars (*$p < 0.05$, **$p < 0.01$, and ***$p < 0.001$).

several actin bundles coming from different directions.[51,52] The formation of these actin patterns, such as asters or stars, has been hypothesized to be associated with high levels of intrinsic mechanical stress within the cortical network.[53,54] They may, therefore, indicate a high-tension state for the stellate cells residing on the S2, S3, and L3 patterns.

The stellate cells cultured on the L2 patterns exhibited a different type of cytoskeletal organization as compared to the stellate cells grown on other patterns. Big peripheral actin stress fibers were observed, while the nuclear region was characterized by a very limited presence of actin fibers or filaments and thus a low value of the elastic modulus (i.e., 8.5 kPa for the sample cell shown in Figure 5g). This suggests a lower contractility and tension of the stellate cells on the L2 pattern as compared to the other patterns. Interestingly, the cells residing on the L2 patterns, in contrast with those cultured on the other patterns (S2, S3, and L3), exhibited mostly a "bottom settling state" (i.e., contact not only with the top of the pillars but also with the substrate between them) (Figure 4a,b). This observation suggests a correlation between the way cells adhere to and settle onto the patterns (i.e., top state or bottom state) and their response in terms of cytoskeletal organization and mechanical properties.

3.2.4. Summary of the Early Cellular Responses on Submicron Pillars. We found a correlation between the initial phase of cell adhesion and the settling state of the cells on the patterned surfaces. While the cells residing on the S2, S3, and L3 surfaces generally only interacted with the tip of the pillars (i.e., exhibited a dominant top settling state), those on the L2 surface interacted with both the pillars and the substrate (i.e., exhibited a dominant bottom settling state) (Figure 4a,b). This is most likely caused by the spatial organization of these pillars, which enables the cells to partially occupy the space between them. Our SCFS results suggest that a similar type of cell–pattern interaction may occur during the initial adhesion phase. Assuming that cells come into contact only with the tip of the pillars when interacting with the S3 and L3 patterns, the significant increase in the work of adhesion observed in the case of S3 as compared to L3 can be explained by the increase in the available surface caused by a higher areal density of the pillars. The increased density of the initial anchoring points could result in a higher density of integrin binding sites, which could give rise, during the later adhesion phases, to a different, potentially faster FA development process.[40,55,56] We did not observe a significant difference in the work of adhesion of the S2 and L2 patterns. This observation, in combination with the results of the SEM analysis, indicates that there is no direct relationship between the density of the pillars and the binding sites in the case of the S2 and L2 patterns. This is because the cells settle differently onto the surface (i.e., dominant top state in the case of S2 and dominant bottom state in the case of L2).

Interestingly, the effects of topography on the initial adhesion force, FA area, and density were visible only on those patterns that exhibited a dominant top state (S2, S3, and L3). No significant difference in the FA area and density as compared to the control surface was observed for the patterns

https://doi.org/10.1021/acsami.1c03687
ACS Appl. Mater. Interfaces 2021, 13, 33767−33781

with a dominant bottom state. Therefore, the patterns influenced the adhesion process and FA development only when the contact between the cells and the pillars was concentrated around the tip of the pillars.

We also found a direct relationship between the cell adhesion, surface wettability, and surface roughness. S3 and L3 were the roughest and most hydrophilic surfaces, and the cells on those patterns exhibited the highest initial adhesion force and the most abundant FA sites after 1 day. Our results are in line with the previous studies showing the positive impact of hydrophilicity[25] and intermediate roughness (i.e., R_a ~ 200 nm) in the submicron range on cell adhesion.[4,57,58]

Furthermore, our results suggest a faster FA formation process on the S3 pattern (Figure 3a). The faster formation of vinculin-rich sites may have been caused not only by the high initial adhesion force on such surfaces but also by the geometry of the pillars (height and interspace). Tall and dense pillars provide a large number of anchoring points (higher work of adhesion), as observed in our SCFS experiments. The high density of the anchoring points could result in a high density of integrin binding sites, which could more easily cluster and develop mature FAs.[56]

The morphology and cytoskeletal organization of the cells on day 1 support the statement regarding the faster formation of mature FAs. The S3 patterns exhibited the highest numbers of stellate cells at day 1, implying the greater coupling of the focal points with F-actin, which normally form in the presence of mature FAs[42,59] and thus indicate a more advanced state of the FA formation process.

The cells cultured on the S3 surfaces with both elongated and stellate morphologies exhibited the highest values of the elastic modulus and the highest degree of cytoskeletal organization, characterized by the presence of thick and dense actin stress fibers in the perinuclear region. This observation suggests a higher contractility and higher tension as compared to the cells interacting with the other patterns, which may be attributed to the different adhesion behavior of the cells residing on this type of surface, as indicated by the initial force and work of adhesion as well as the development and distribution of FAs. This may lead to a higher level of nuclear tension[4,60] and affect subsequent cellular functions. Indeed, previous studies have shown that the presence of dense actin cap fibers is associated with elevated levels of nuclear tension, high chromatin condensation, and YAP nuclear accumulation, resulting in the osteogenic differentiation of MSCs on catecholic polyglycerol coatings with roughness values (R_a) in the range of 150−300 nm.[4]

The next question was whether our findings regarding the early adhesion, morphology, and mechanical properties of preosteoblasts affect the subsequent cellular functions. Therefore, a long-term experiment was performed to investigate the ECM formation by preosteoblast cells.

3.3. Effects of the Patterns on the ECM. One of the essential ECM proteins expressed by mature osteoblasts is OPN,[61] which is further enhanced by applying mechanical stress.[62] We, therefore, analyzed the level of OPN expression for the specimens from different experimental groups using both osteogenic and nonosteogenic media after 21 days of cell culture. On flat controls, OPN was expressed only in the osteogenic medium (Figure 6b). In the osteogenic condition, the surfaces patterned with the tallest pillars (i.e., S3 and L3, height = 1000 nm) significantly upregulated the expression of OPN as compared to the other patterns and the control group (Figure 6a,c). In addition, a slight (not significant) increase in the OPN expression compared to the control surface was observed for the S2 group, while the other patterns did not show any difference as compared to the control group (Figure 6c). A difference in the OPN expression after 21 days was observed only on those patterns (S2, S3, and L3) for which an increased area and density of FAs were observed after 1 day (Figure 6f) and where cells mostly interacted with the top region of the pillars (dominant top state). This finding supports the presence of a relationship between the capability of the cells to rapidly form mature FAs and the subsequent matrix mineralization process. The S3 pattern, for which we found the strongest cell adhesion and the highest elastic modulus values in the perinuclear areas, also exhibited the highest level of OPN expression, further supporting the hypothesis that a direct relationship exists between the early cell adhesion behavior and the late matrix mineralization process. We did not, however, detect a significant difference between S3 and L3 (pillars with a larger interspacing of 1000 nm) under the osteogenic conditions (Figure 6a,c).

To isolate the effects of the surface patterns from those of the osteogenic supplements, we repeated the experiments for the S3, L3, and control groups under nonosteogenic conditions. The difference between the OPN expression of the S3 and L3 groups was statistically significant when using a nonosteogenic medium (Figure 6d,e). The differential effects of the patterns with different geometries on the OPN expression could, therefore, be more easily detected when the influence of the osteogenic supplements was removed. These findings reveal possible osteoinductive properties of the S3 pattern.

The combined use of different techniques allowed us to unravel the relationships between the early and late indicators of the response of preosteoblasts to submicron surface patterns. On the most potent pattern, that is, the S3 pattern, the initial work of adhesion and the area of FA sites (vinculin) were upregulated, which in turn increased the elastic modulus of the cells by stretching actin stress fibers in all directions (Figure 6f). As a result, the highest amount of OPN expression was observed (Figure 6e). Thus, the quantitative and systematic approach used in our study suggests that the earlier markers related to the adhesion phase (e.g., adhesion strength and cell mechanical properties) may be useful for predicting the osteogenic potential of patterned biomaterials.

The geometry and spacing of the submicron and nanopillars are known to influence the extracellular proteins expressed by preosteoblasts.[63] At the nanoscale, shorter pillars enhanced the bone matrix nodules in hMCSs.[9] While at the submicron scale, we observed an opposite trend. The tall and dense submicron pillars were the most potent physical stimuli to alter the response and function of preosteoblast cells. Furthermore, the roughness of the osteogenic pattern identified in our study is in the range of the roughness values (150−450 nm) that have been found in the literature to enhance the osteogenic differentiation of osteoblasts and MSCs.[4,64]

In addition to the surface design, the substrate stiffness can influence the response of cells. It is known that in soft materials such as hydrogels, a higher stiffness is needed to favor osteogenic differentiation in hMSC and preosteoblasts.[65,66] On the other hand, the scale of surface topographies affects osteogenic differentiation on very stiff substrates, such as titanium. For example, at the nanoscale, short titania pillars (around 15 nm in height) have been found to be effective for

https://doi.org/10.1021/acsami.1c03687
ACS Appl. Mater. Interfaces 2021, 13, 33767−33781

the mineralization of MSCs.[9] At the submicron scale, roughness values around 150−450 nm have been shown to stimulate the adhesion and osteogenesis of osteoblasts and MSCs.[4,64] By comparison, macroscale roughness (1050 nm) tend to attenuate the osteogenic mineralization of MSCs[4] and the formation of FAs in osteoblasts (R_a = 2.190−3.400 μm).[67]

Substrate stiffness and topographies can induce intracellular tension by promoting the polymerization of actin and increasing actomyosin forces.[68,69] Increasing the stiffness of the substrate activates RhoA/ROCK signaling pathways, leading to the enhanced osteogenesis of hMSCs.[68,70] The presence of stretch and tension in the osteoblast cytoskeleton leads to the activation of the mechanocoupling phase and is a messenger of the mechanotransduction process.[62] A direct mechanotransduction pathway may be activated by the S3 pattern via integrin clustering, followed by the signal transduction through the cytoskeleton elements toward the nucleus where mechanoactuators activate the mechanosensitive genes. These mechanotransduction pathways include kinase pathways that involve the phosphorylation of kinase proteins, such as FA kinase, and the subsequent upregulation of late osteogenic markers, such as the OPN gene in preosteoblasts.[12,62] Further research is required to gain insights into the mechanotransduction pathways activated by such a patterned surface.

4. CONCLUSIONS

We performed a systematic study on the effects of the design parameters of 3D-printed submicron pillars on the response of preosteoblasts from initial adhesion to the formation of the extracellular matrix. This included the single-cell measurement of the adhesion parameters (i.e., adhesion force and work of adhesion), a study of cell morphology and cytoskeletal organization, mapping of the elastic modulus within individual cells, and expression of late osteogenic markers (i.e., OPN). The adhesion of cells and the subsequent formation of FAs were positively modulated by the surface topography only when the pillars were tall and dense enough, in which case the cells settled onto the surface in the "top state". Furthermore, the cells interacting with tall and dense pillars were characterized by numerous thick actin stress fibers in the perinuclear region and the upregulation of OPN. Our findings reveal previously undocumented mechanistic pathways through which submicron pillars with specific geometries and spatial organizations initiate a cascade of events that regulate the cell response starting from initial adhesion and continuing all the way to matrix mineralization. These findings pave the way toward the discovery of early and quantifiable markers capable of predicting the osteogenic potential of biomaterials. This improved understanding of how the design parameters of submicron pillars influence the bone tissue regeneration process could inform the future designs of instructive surfaces, thereby enhancing the osseointegration of future orthopedic implants.

AUTHOR INFORMATION

Corresponding Authors

Mahdiyeh Nouri-Goushki − *Department of Biomechanical Engineering, Faculty of Mechanical, Maritime, and Materials Engineering, Delft University of Technology (TU Delft), 2628 CD Delft, The Netherlands*; orcid.org/0000-0003-1665-9144; Email: m.nourigoushki@tudelft.nl, mhd.nouri71@gmail.com

Livia Angeloni − *Department of Biomechanical Engineering, Faculty of Mechanical, Maritime, and Materials Engineering, Delft University of Technology (TU Delft), 2628 CD Delft, The Netherlands; Department of Precision and Microsystems Engineering, Faculty of Mechanical, Maritime, and Materials Engineering, Delft University of Technology (TU Delft), 2628 CD Delft, The Netherlands*; Phone: +31-152786980; Email: l.angeloni@tudelft.nl

Lidy E. Fratila-Apachitei − *Department of Biomechanical Engineering, Faculty of Mechanical, Maritime, and Materials Engineering, Delft University of Technology (TU Delft), 2628 CD Delft, The Netherlands*; orcid.org/0000-0002-7341-4445; Email: E.L.Fratila-Apachitei@tudelft.nl

Authors

Khashayar Modaresifar − *Department of Biomechanical Engineering, Faculty of Mechanical, Maritime, and Materials Engineering, Delft University of Technology (TU Delft), 2628 CD Delft, The Netherlands*; orcid.org/0000-0002-0391-8541

Michelle Minneboo − *Department of Biomechanical Engineering, Faculty of Mechanical, Maritime, and Materials Engineering, Delft University of Technology (TU Delft), 2628 CD Delft, The Netherlands*

Pouyan E. Boukany − *Department of Chemical Engineering, Delft University of Technology (TU Delft), 2629 HZ Delft, The Netherlands*

Mohammad J. Mirzaali − *Department of Biomechanical Engineering, Faculty of Mechanical, Maritime, and Materials Engineering, Delft University of Technology (TU Delft), 2628 CD Delft, The Netherlands*; orcid.org/0000-0002-5349-6922

Murali K. Ghatkesar − *Department of Precision and Microsystems Engineering, Faculty of Mechanical, Maritime, and Materials Engineering, Delft University of Technology (TU Delft), 2628 CD Delft, The Netherlands*

Amir A. Zadpoor − *Department of Biomechanical Engineering, Faculty of Mechanical, Maritime, and Materials Engineering, Delft University of Technology (TU Delft), 2628 CD Delft, The Netherlands*; orcid.org/0000-0003-3234-2112

Complete contact information is available at: https://pubs.acs.org/10.1021/acsami.1c03687

Author Contributions

M.N.-G. and L.A. are joint first authors; L.E.F.-A. and A.A.Z. are joint senior authors. M.N.-G., K.M., L.E.F.-A., and A.A.Z. conceptualized the study; M.N.-G. designed, fabricated, and characterized the patterns, and performed the early cell experiments and analyses under the supervision of L.E.F.-A. and A.A.Z.; L.A. performed AFM and SCSF experiments under the supervision of M.K.G., L.E.F.-A, and P.E.B.; M.N.-G. and K.M. performed SEM imaging; K.M. performed the OPN experiments; M.M. developed cell culture protocols; M.J.M. performed FEM simulation and statistical analysis; M.N.-G. and L.A. wrote the first draft; and all authors revised the manuscript.

Notes

The authors declare no competing financial interest.

The raw/processed data required to reproduce these findings cannot be shared at this time as the data also form a part of an ongoing study.

https://doi.org/10.1021/acsami.1c03687
ACS Appl. Mater. Interfaces 2021, 13, 33767−33781

■ ACKNOWLEDGMENTS

The research leading to these results has received funding from the European Research Council under the ERC grant agreement no [677575]. Moreover, our research was partially funded by grants from TU Delft (Cohesion grant "Diagnosis" of soft matter on nanopatterned surfaces for better implants) and the European Union's Horizon 2020 research and innovation program under the Marie Skłodowska Curie (LEaDing Fellows grant no. 707404). We would like to thank Prof. Dr. Urs Staufer (Department of Precision and Microsystems Engineering, TU Delft) for his comments on the manuscript, Dr. Daniel Fan (Department of Precision and Microsystems Engineering, TU Delft) for the technical assistance with the Nanoscribe equipment, Dr. Cornelis W. Hagen (Department of Imaging Physics, TU Delft) for the access to the SEM equipment, and Dr. Monique A. van der Veen (Department of Chemical Engineering, TU Delft), Bart van der Linden (Department of Chemical Engineering, TU Delft), and Bart Boshuizen (Department of Chemical Engineering, TU Delft) for the technical assistance with the ATR-FTIR and XPS equipment.

■ REFERENCES

(1) Khang, D.; Lu, J.; Yao, C.; Haberstroh, K. M.; Webster, T. J. The Role of Nanometer and Sub-micron Surface Features on Vascular and Bone Cell Adhesion on Titanium. *Biomaterials* **2008**, *29*, 970−983.

(2) Mirzaali, M. J.; Van Dongen, I. C. P.; Tümer, N.; Weinans, H.; Yavari, S. A.; Zadpoor, A. A. In-Silico Quest for Bactericidal but Non-Cytotoxic Nanopatterns. *Nanotechnology* **2018**, *29*, 43LT02.

(3) McWhorter, F. Y.; Wang, T.; Nguyen, P.; Chung, T.; Liu, W. F. Modulation of Macrophage Phenotype by Cell Shape. *Proc. Natl. Acad. Sci. U.S.A.* **2013**, *110*, 17253−17258.

(4) Hou, Y.; Xie, W.; Yu, L.; Camacho, L. C.; Nie, C.; Zhang, M.; Haag, R.; Wei, Q. Surface Roughness Gradients Reveal Topography-Specific Mechanosensitive Responses in Human Mesenchymal Stem Cells. *Small* **2020**, *16*, 1905422.

(5) Higgins, S. G.; Becce, M.; Belessiotis-Richards, A.; Seong, H.; Sero, J. E.; Stevens, M. M. High-Aspect-Ratio Nanostructured Surfaces as Biological Metamaterials. *Adv. Mater.* **2020**, *32*, 1903862.

(6) Dalby, M. J.; Gadegaard, N.; Tare, R.; Andar, A.; Riehle, M. O.; Herzyk, P.; Wilkinson, C. D. W.; Oreffo, R. O. C. The Control of Human Mesenchymal Cell Differentiation Using Nanoscale Symmetry and Disorder. *Nat. Mater.* **2007**, *6*, 997−1003.

(7) Dobbenga, S.; Fratila-Apachitei, L. E.; Zadpoor, A. A. Nanopattern-Induced Osteogenic Differentiation of Stem Cells−A Systematic Review. *Acta Biomater.* **2016**, *46*, 3−14.

(8) Lovmand, J.; Justesen, J.; Foss, M.; Lauridsen, R. H.; Lovmand, M.; Modin, C.; Besenbacher, F.; Pedersen, F. S.; Duch, M. The Use of Combinatorial Topographical Libraries for the Screening of Enhanced Osteogenic Expression and Mineralization. *Biomaterials* **2009**, *30*, 2015−2022.

(9) Sjöström, T.; Dalby, M. J.; Hart, A.; Tare, R.; Oreffo, R. O. C.; Su, B. Fabrication of Pillar-Like Titania Nanostructures on Titanium and their Interactions with Human Skeletal Stem Cells. *Acta Biomater.* **2009**, *5*, 1433−1441.

(10) McNamara, L. E.; Sjöström, T.; Burgess, K. E. V.; Kim, J. J. W.; Liu, E.; Gordonov, S.; Moghe, P. V.; Meek, R. M. D.; Oreffo, R. O. C.; Su, B.; Dalby, M. J. Skeletal Stem Cell Physiology on Functionally Distinct Titania Nanotopographies. *Biomaterials* **2011**, *32*, 7403−7410.

(11) Tan, J. L.; Tien, J.; Pirone, D. M.; Gray, D. S.; Bhadriraju, K.; Chen, C. S. Cells Lying on a Bed of Microneedles: an Approach to Isolate Mechanical Force. *Proc. Natl. Acad. Sci. U.S.A.* **2003**, *100*, 1484−1489.

(12) Gautrot, J. E.; Malmström, J.; Sundh, M.; Margadant, C.; Sonnenberg, A.; Sutherland, D. S. The Nanoscale Geometrical Maturation of Focal Adhesions Controls Stem Cell Differentiation and Mechanotransduction. *Nano Lett.* **2014**, *14*, 3945−3952.

(13) Kwon, K. W.; Choi, S. S.; Kim, B.; Lee, S. N.; Park, M. C.; Kim, P.; Lee, S. H.; Park, S. H.; Suh, K. Y. A Microfluidic Flow Sensor for Measuring Cell Adhesion. *2006 5th IEEE Conference on Sensors*; IEEE, 2006; pp 105−108.

(14) Zorlutuna, P.; Rong, Z.; Vadgama, P.; Hasirci, V. Influence of Nanopatterns on Endothelial Cell Adhesion: Enhanced Cell Retention under Shear Stress. *Acta Biomater.* **2009**, *5*, 2451−2459.

(15) Galbraith, C. G.; Sheetz, M. P. A Micromachined Device Provides a New Bend on Fibroblast Traction Forces. *Proc. Natl. Acad. Sci. U.S.A.* **1997**, *94*, 9114−9118.

(16) Roy, P.; Rajfur, Z.; Pomorski, P.; Jacobson, K. Microscope-Based Techniques to Study Cell Adhesion and Migration. *Nat. Cell Biol.* **2002**, *4*, E91−E96.

(17) Bao, G.; Suresh, S. Cell and Molecular Mechanics of Biological Materials. *Nat. Mater.* **2003**, *2*, 715−725.

(18) Taubenberger, A. V.; Woodruff, M. A.; Bai, H.; Muller, D. J.; Hutmacher, D. W. The Effect of Unlocking RGD-motifs in Collagen I on Pre-osteoblast Adhesion and Differentiation. *Biomaterials* **2010**, *31*, 2827−2835.

(19) Jiang, L.; Sun, Z.; Chen, X.; Li, J.; Xu, Y.; Zu, Y.; Hu, J.; Han, D.; Yang, C. Cells Sensing Mechanical Cues: Stiffness Influences the Lifetime of Cell-Extracellular Matrix Interactions by Affecting the Loading Rate. *ACS Nano* **2016**, *10*, 207−217.

(20) Markwardt, J.; Friedrichs, J.; Werner, C.; Davids, A.; Weise, H.; Lesche, R.; Weber, A.; Range, U.; Meißner, H.; Lauer, G.; Reitemeier, B. Experimental Study on the Behavior of Primary Human Osteoblasts on Laser-Cused Pure Titanium Surfaces. *J. Biomed. Mater. Res., Part A* **2014**, *102*, 1422−1430.

(21) Naganuma, T. The Relationship Between Cell Adhesion Force Activation on Nano/Micro-Topographical Surfaces and Temporal Dependence of Cell Morphology. *Nanoscale* **2017**, *9*, 13171−13186.

(22) Grau, M.; Matena, J.; Teske, M.; Petersen, S.; Aliuos, P.; Roland, L.; Grabow, N.; Murua Escobar, H.; Gellrich, N.-C.; Haferkamp, H.; Nolte, I. In Vitro Evaluation of PCL and P(3HB) as Coating Materials for Selective Laser Melted Porous Titanium Implants. *Materials* **2017**, *10*, 1344.

(23) Bertoncini, P.; Le Chevalier, S.; Lavenus, S.; Layrolle, P.; Louarn, G. Early Adhesion of Human Mesenchymal Stem Cells on TiO2 Surfaces Studied by Single-Cell Force Spectroscopy Measurements. *J. Mol. Recognit.* **2012**, *25*, 262−269.

(24) Cimmino, C.; Rossano, L.; Netti, P. A.; Ventre, M. Spatio-Temporal Control of Cell Adhesion: Toward Programmable Platforms to Manipulate Cell Functions and Fate. *Front. Bioeng. Biotechnol.* **2018**, *6*, 190.

(25) Nouri-Goushki, M.; Mirzaali, M. J.; Angeloni, L.; Fan, D.; Minneboo, M.; Ghatkesar, M. K.; Staufer, U.; Fratila-Apachitei, L. E.; Zadpoor, A. A. 3D Printing of Large Areas of Highly Ordered Submicron Patterns for Modulating Cell Behavior. *ACS Appl. Mater. Interfaces* **2020**, *12*, 200−208.

(26) Nouri-Goushki, M.; Sharma, A.; Sasso, L.; Zhang, S.; Van der Eerden, B. C. J.; Staufer, U.; Fratila-Apachitei, L. E.; Zadpoor, A. A. Submicron Patterns-on-a-Chip: Fabrication of a Microfluidic Device Incorporating 3D Printed Surface Ornaments. *ACS Biomater. Sci. Eng.* **2019**, *5*, 6127−6136.

(27) Taubenberger, A.; Cisneros, D. A.; Friedrichs, J.; Puech, P.-H.; Muller, D. J.; Franz, C. M. Revealing Early Steps of $\alpha 2\beta 1$ Integrin-mediated Adhesion to Collagen Type I by Using Single-Cell Force Spectroscopy. *Mol. Biol. Cell* **2007**, *18*, 1634−1644.

(28) Strohmeyer, N.; Bharadwaj, M.; Costell, M.; Fässler, R.; Müller, D. J. Fibronectin-Bound $\alpha 5\beta 1$ Integrins Sense Load and Signal to Reinforce Adhesion in Less than a Second. *Nat. Mater.* **2017**, *16*, 1262−1270.

(29) Changede, R.; Xu, X.; Margadant, F.; Sheetz, M. P. Nascent Integrin Adhesions Form on All Matrix Rigidities after Integrin Activation. *Dev. Cell* **2015**, *35*, 614−621.

(30) Belikov, S.; Alexander, J.; Wall, C.; Yermolenko, I.; Magonov, S.; Malovichko, I. Thermal Tune Method for AFM Oscillatory

https://doi.org/10.1021/acsami.1c03687
ACS Appl. Mater. Interfaces 2021, 13, 33767−33781

Resonant Imaging in Air and Liquid. *American Control Conference, 4–6 June, 2014*, 2014; pp 1009–1014.
(31) Sneddon, I. N. The Relation Between Load and Penetration in the Axisymmetric Boussinesq Problem for a Punch of Arbitrary Profile. *Int. J. Eng. Sci.* **1965**, *3*, 47–57.
(32) Horzum, U.; Ozdil, B.; Pesen-Okvur, D. Step-by-Step Quantitative Analysis of Focal Adhesions. *MethodsX* **2014**, *1*, 56–59.
(33) Busscher, H. J.; Van Pelt, A. W. J.; De Boer, P.; De Jong, H. P.; Arends, J. The Effect of Surface Roughening of Polymers on Measured Contact Angles of Liquids. *Colloids Surf.* **1984**, *9*, 319–331.
(34) Lampin, M.; Warocquier-Clérout, R.; Legris, C.; Degrange, M.; Sigot-Luizard, M. F. Correlation between Substratum Roughness and Wettability, Cell Adhesion, and Cell Migration. *J. Biomed. Mater. Res.* **1997**, *36*, 99–108.
(35) Benoit, M.; Gaub, H. E. Measuring Cell Adhesion Forces with the Atomic Force Microscope at the Molecular Level. *Cells Tissues Organs* **2002**, *172*, 174–189.
(36) Friedrichs, J.; Legate, K. R.; Schubert, R.; Bharadwaj, M.; Werner, C.; Müller, D. J.; Benoit, M. A Practical Guide to Quantify Cell Adhesion Using Single-Cell Force Spectroscopy. *Methods* **2013**, *60*, 169–178.
(37) Ferrari, M.; Cirisano, F.; Morán, M. C. Mammalian Cell Behavior on Hydrophobic Substrates: Influence of Surface Properties. *Colloids Interfaces* **2019**, *3*, 48.
(38) Goushki, M. N.; Mousavi, S. A.; Abdekhodaie, M. J.; Sadeghi, M. Free Radical Graft Polymerization of 2-Hydroxyethyl Methacrylate and Acrylic Acid on the Polysulfone Membrane Surface Through Circulation of Reaction Media to Improve its Performance and Hemocompatibility Properties. *J. Membr. Sci.* **2018**, *564*, 762–772.
(39) Gauthier, N. C.; Masters, T. A.; Sheetz, M. P. Mechanical Feedback between Membrane Tension and Dynamics. *Trends Cell Biol.* **2012**, *22*, 527–535.
(40) Kuo, C. W.; Chueh, D.-Y.; Chen, P. Investigation of Size–Dependent Cell Adhesion on Nanostructured Interfaces. *J. Nanobiotechnol.* **2014**, *12*, 54.
(41) Zaidel-Bar, R.; Cohen, M.; Addadi, L.; Geiger, B. Hierarchical Assembly of Cell–Matrix Adhesion Complexes. *Biochem. Soc. Trans.* **2004**, *32*, 416–420.
(42) Zhukova, Y.; Hiepen, C.; Knaus, P.; Osterland, M.; Prohaska, S.; Dunlop, J. W. C.; Fratzl, P.; Skorb, E. V. The Role of Titanium Surface Nanostructuring on Preosteoblast Morphology, Adhesion, and Migration. *Adv. Healthcare Mater.* **2017**, *6*, 1601244.
(43) Zhou, J.; Zhang, X.; Sun, J.; Dang, Z.; Li, J.; Li, X.; Chen, T. The Effects of Surface Topography of Nanostructure Arrays on Cell Adhesion. *Phys. Chem. Chem. Phys.* **2018**, *20*, 22946–22951.
(44) Bucaro, M. A.; Vasquez, Y.; Hatton, B. D.; Aizenberg, J. Fine-Tuning the Degree of Stem Cell Polarization and Alignment on Ordered Arrays of High-Aspect-Ratio Nanopillars. *ACS Nano* **2012**, *6*, 6222–6230.
(45) Buch-Månson, N.; Kang, D.-H.; Kim, D.; Lee, K. E.; Yoon, M.-H.; Martinez, K. L. Mapping Cell Behavior Across a Wide Range of Vertical Silicon Nanocolumn Densities. *Nanoscale* **2017**, *9*, 5517–5527.
(46) Stricker, J.; Aratyn-Schaus, Y.; Oakes, P. W.; Gardel, M. L. Spatiotemporal Constraints on the Force-Dependent Growth of Focal Adhesions. *Biophys. J.* **2011**, *100*, 2883–2893.
(47) Trichet, L.; Le Digabel, J.; Hawkins, R. J.; Vedula, S. R. K.; Gupta, M.; Ribrault, C.; Hersen, P.; Voituriez, R.; Ladoux, B. Evidence of a Large-Scale Mechanosensing Mechanism for Cellular Adaptation to Substrate Stiffness. *Proc. Natl. Acad. Sci. U.S.A.* **2012**, *109*, 6933.
(48) Roduit, C.; Sekatski, S.; Dietler, G.; Catsicas, S.; Lafont, F.; Kasas, S. Stiffness Tomography by Atomic Force Microscopy. *Biophys. J.* **2009**, *97*, 674–677.
(49) Angeloni, L.; Reggente, M.; Passeri, D.; Natali, M.; Rossi, M. Identification of Nanoparticles and Nanosystems in Biological Matrices with Scanning Probe Microscopy. *WIREs Nanomed. Nanobiotechnol.* **2018**, *10*, No. e1521.
(50) Maninova, M.; Caslavsky, J.; Vomastek, T. The Assembly and Function of Perinuclear Actin Cap in Migrating Cells. *Protoplasma* **2017**, *254*, 1207–1218.
(51) Fritzsche, M.; Li, D.; Colin-York, H.; Chang, V. T.; Moeendarbary, E.; Felce, J. H.; Sezgin, E.; Charras, G.; Betzig, E.; Eggeling, C. Self-Organizing Actin Patterns Shape Membrane Architecture but not Cell Mechanics. *Nat. Commun.* **2017**, *8*, 14347.
(52) Guerrero, C. R.; Garcia, P. D.; Garcia, R. Subsurface Imaging of Cell Organelles by Force Microscopy. *ACS Nano* **2019**, *13*, 9629–9637.
(53) Haviv, L.; Brill-Karniely, Y.; Mahaffy, R.; Backouche, F.; Ben-Shaul, A.; Pollard, T. D.; Bernheim-Groswasser, A. Reconstitution of the Transition from Lamellipodium to Filopodium in a Membrane-Free System. *Proc. Natl. Acad. Sci. U.S.A.* **2006**, *103*, 4906.
(54) Soares e Silva, M.; Depken, M.; Stuhrmann, B.; Korsten, M.; MacKintosh, F. C.; Koenderink, G. H. Active Multistage Coarsening of Actin Networks Driven by Myosin Motors. *Proc. Natl. Acad. Sci. U.S.A.* **2011**, *108*, 9408.
(55) Cavalcanti-Adam, E. A.; Volberg, T.; Micoulet, A.; Kessler, H.; Geiger, B.; Spatz, J. P. Cell Spreading and Focal Adhesion Dynamics Are Regulated by Spacing of Integrin Ligands. *Biophys. J.* **2007**, *92*, 2964–2974.
(56) Jansen, K. A.; Donato, D. M.; Balcioglu, H. E.; Schmidt, T.; Danen, E. H. J.; Koenderink, G. H. A Guide to Mechanobiology: Where Biology and Physics Meet. *Biochim. Biophys. Acta, Mol. Cell Res.* **2015**, *1853*, 3043–3052.
(57) Lerebours, A.; Vigneron, P.; Bouvier, S.; Rassineux, A.; Bigerelle, M.; Egles, C. Additive Manufacturing Process Creates Local Surface Roughness Modifications Leading to Variation in Cell Adhesion on Multifaceted TiAl6V4 Samples. *Bioprinting* **2019**, *16*, No. e00054.
(58) Wu, C.; Chen, M.; Zheng, T.; Yang, X. Effect of Surface Roughness on the Initial Response of MC3T3-E1 Cells Cultured on Polished Titanium Alloy. *Bio-Med. Mater. Eng.* **2015**, *26*, S155–S164.
(59) Kulangara, K.; Leong, K. W. Substrate Topography Shapes Cell Function. *Soft Matter* **2009**, *5*, 4072–4076.
(60) Buxboim, A.; Irianto, J.; Swift, J.; Athirasala, A.; Shin, J.-W.; Rehfeldt, F.; Discher, D. E. Coordinated Increase of Nuclear Tension and Lamin-A with Matrix Stiffness Outcompetes Lamin-B Receptor that Favors Soft Tissue Phenotypes. *Mol. Biol. Cell* **2017**, *28*, 3333–3348.
(61) Zhu, M.; Ye, H.; Fang, J.; Zhong, C.; Yao, J.; Park, J.; Lu, X.; Ren, F. Engineering High-Resolution Micropatterns Directly onto Titanium with Optimized Contact Guidance to Promote Osteogenic Differentiation and Bone Regeneration. *ACS Appl. Mater. Interfaces* **2019**, *11*, 43888–43901.
(62) Stewart, S.; Darwood, A.; Masouros, S.; Higgins, C.; Ramasamy, A. Mechanotransduction in Osteogenesis. *Bone Jt. Res.* **2020**, *9*, 1–14.
(63) Ghezzi, B.; Lagonegro, P.; Fukata, N.; Parisi, L.; Calestani, D.; Galli, C.; Salviati, G.; Macaluso, G. M.; Rossi, F. Sub-Micropillar Spacing Modulates the Spatial Arrangement of Mouse MC3T3-E1 Osteoblastic Cells. *Nanomaterials* **2019**, *9*, 1701.
(64) Khang, D.; Choi, J.; Im, Y.-M.; Kim, Y.-J.; Jang, J.-H.; Kang, S. S.; Nam, T.-H.; Song, J.; Park, J.-W. Role of Subnano-, Nano- and Submicron-Surface Features on Osteoblast Differentiation of Bone Marrow Mesenchymal Stem Cells. *Biomaterials* **2012**, *33*, 5997–6007.
(65) Sun, M.; Chi, G.; Xu, J.; Tan, Y.; Xu, J.; Lv, S.; Xu, Z.; Xia, Y.; Li, L.; Li, Y. Extracellular Matrix Stiffness Controls Osteogenic Differentiation of Mesenchymal Stem Cells Mediated by Integrin α5. *Stem Cell Res. Ther.* **2018**, *9*, 52.
(66) Lee, H.-S.; Kang, J.-I.; Chung, W.-J.; Lee, D. H.; Lee, B. Y.; Lee, S.-W.; Yoo, S. Y. Engineered Phage Matrix Stiffness-Modulating Osteogenic Differentiation. *ACS Appl. Mater. Interfaces* **2018**, *10*, 4349–4358.
(67) Anselme, K.; Bigerelle, M.; Noel, B.; Dufresne, E.; Judas, D.; Iost, A.; Hardouin, P. Qualitative and Quantitative Study of Human Osteoblast Adhesion on Materials with Various Surface Roughnesses. *J. Biomed. Mater. Res.* **2000**, *49*, 155–166.

https://doi.org/10.1021/acsami.1c03687
ACS Appl. Mater. Interfaces 2021, 13, 33767–33781

(68) Yang, Y.; Wang, K.; Gu, X.; Leong, K. W. Biophysical Regulation of Cell Behavior-Cross Talk between Substrate Stiffness and Nanotopography. *Engineering* **2017**, *3*, 36−54.
(69) Ghibaudo, M.; Saez, A.; Trichet, L.; Xayaphoummine, A.; Browaeys, J.; Silberzan, P.; Buguin, A.; Ladoux, B. Traction Forces and Rigidity Sensing Regulate Cell Functions. *Soft Matter* **2008**, *4*, 1836−1843.
(70) Keung, A. J.; de Juan-Pardo, E. M.; Schaffer, D. V.; Kumar, S. Rho GTPases Mediate the Mechanosensitive Lineage Commitment of Neural Stem Cells. *Stem Cells* **2011**, *29*, 1886−1897.

https://doi.org/10.1021/acsami.1c03687
ACS Appl. Mater. Interfaces 2021, 13, 33767−33781